First Vegetation Optical Depth Mapping from Sentinel-1 C-band SAR Data over Crop Fields

Mohammad Hajj, Nicolas Baghdadi, Jean-Pierre Wigneron, Mehrez Zribi, Clément Albergel, Jean-Christophe Calvet, Ibrahim Fayad

remote sensing

MDPI

Article

First Vegetation Optical Depth Mapping from Sentinel-1 C-band SAR Data over Crop Fields

Mohammad El Hajj [1,*], Nicolas Baghdadi [1], Jean-Pierre Wigneron [2], Mehrez Zribi [3], Clément Albergel [4], Jean-Christophe Calvet [4] and Ibrahim Fayad [1]

1 IRSTEA, University of Montpellier, UMR TETIS, 500 rue François Breton, 34093 Montpellier CEDEX 5, France; nicolas.baghdadi@teledetection.fr (N.B.); ibrahim.fayad@irstea.fr (I.F.)
2 INRA, Centre INRA Bordeaux Aquitaine, URM1391 ISPA, F-33140 Villenave d'Ornon, France; jean-pierre.wigneron@inra.fr
3 Centre d'Etudes Spatiales de la BIOsphère (CESBIO), Université de Toulouse, CNES/CNRS/IRD/UPS/INRA, 18 av. Edouard Belin, bpi 2801, 31401 Toulouse CEDEX 9, France; mehrez.zribi@ird.fr
4 CNRM, Université de Toulouse, Météo-France, CNRS, 31057 Toulouse, France; clement.albergel@meteo.fr (C.A.); jean-christophe.calvet@meteo.fr (J.-C.C.)
* Correspondence: mohammad.el-hajj@teledetection.com or elhajj.moha@gmail.com

Received: 8 September 2019; Accepted: 20 November 2019; Published: 25 November 2019

Abstract: Monitoring crop status at plot scale in agricultural areas is essential for crop and irrigation management and yield optimization. The Vegetation Optical Depth (VOD) of canopy is directly related to the canopy water content, and thus, it represents an effective tool for crop health monitoring. Currently, VOD is provided at low spatial resolution which makes these estimations useless for vegetation monitoring at plot scale. Therefore, the aim of this study is to provide the first approach to estimate VOD at plot scale for non-irrigated plots from C-band Sentinel-1 (S1) Synthetic Aperture Radar (SAR) data. The proposed approach was tested on a study site of 50 km × 50 km located in Catalonia, Spain. VOD estimates were provided for two crop growth cycles of non-irrigated crop types (barley, fallow, oat, wheat, and rapeseed). The relevance of VOD estimates was investigated for both growth cycles using temporal profiles of the Normalized Difference Vegetation Index (NDVI). It is shown that the temporal dynamics of VOD values computed from VV polarization fits that of NDVI with a medium to good coefficient of determination (R^2 ranging from 0.39 to 0.61 for barley, fallow, oat, and wheat respectively). However, during the beginning of the senescence period in both cycles (mainly in May for winter crops), VOD decreases with the decrease in Vegetation Water Content (VWC) while NDVI keeps increasing as photosynthetic activity continues developing. This illustrates the importance of VOD in crop water loss (stress and/or transpiration) monitoring. The potential of VOD to spot water loss in vegetation is also demonstrated as the evening (18h00) VOD values are lower than those of morning (06h00) due to high daytime temperature that reduces water content in vegetation. Finally, it is shown that VOD values computed from VH polarization are not correlated with NDVI.

Keywords: Vegetation optical depth; Sentinel-1; Sentinel-2; Crops

1. Introduction

According to United Nations, the world population will reach 9.7 billion by 2050. As global air temperature is rising and water scarcity is pushing, maintaining food security for the next generations is certainly a challenge. Tools and solutions should then be developed to adapt agricultural practices to future climate and water conditions, which are likely to not be favorable for having enough food production and to precisely predict the impact of agricultural practices and weather changes on crop

yield. Currently, several agronomic models have been developed in order predict the yield, based on several parameters including, but not limited to, weather conditions and agricultural practices. Such models can predict potential stress and thus can aid decision makers to take actions. For reliable predictions, the calibration of these models, by ground truth data, is a must. As in-situ sensors are limited to crop or field scale, remote sensing, on the other hand, is an effective tool in providing observations on larger scales, with high temporal resolution (6 days of revisit time for Sentinel). In addition to feeding crop models, remote sensing observations can save yield by early detecting the presence of crop diseases and thus could assist farmers for better interventions.

Monitoring crop growth and the state of vegetation is needed for better irrigation management and for optimizing yield. Optical observations at visible and near-infrared wavelengths are commonly used for crop monitoring and crop parameter estimation [1–5]. However, optical observations from space cannot ensure continuous crop monitoring since they are useless in the presence of clouds. Microwave remote sensing at low frequencies is able to operate in all weather conditions and can complement optical observations by monitoring the temporal change in the Vegetation Water Content (VWC). Because a large fraction of the crop biomass consists of water, VWC is related to the amount of fresh biomass and to the vegetation water status.

Several studies have shown that the Vegetation Optical Depth (VOD) derived from microwave data can be used to monitor crops [6–13]. The optical depth of crops is a measure of how opaque a canopy is to microwave radiation passing through it and it is directly related to VWC as well as to instrumental parameters (incidence angle, polarization, and frequency) [6,14–16]. Currently, several VOD products at low spatial resolution are provided from the C-band ASCAT (Advanced SCATterometer), AMSR-E & -2 (Advanced Microwave Scanning Radiometer), and from L-band radiometers such as, SMOS (Soil Moisture and Ocean Salinity) and SMAP (Soil moisture Active and Passive) [6–13,17]. These VOD products were evaluated by several authors. For instance, Patton et al. [12] and Lawrence [10] found that changes in SMOS VOD over croplands in the USA are consistent with the crop cycle: VOD increases during the growing season and decreases during the senescence. Moreover, Lawrence [10] assessed the relationship between SMOS VOD and crops (wheat hay and corn) optical indices including the Normalized Difference Vegetation Index (NDVI), Enhanced Vegetation Index (EVI), Leaf Area Index (LAI), and Normalized difference Water Index (NDWI). They found that VOD is correlated with theses optical indices with a coefficient of determination (R^2) of about 0.33. Chapparo et al. [18] assessed the relationship between SMAP VOD and crops yield (barley, bean, canola, corn, flaxseed, lentils, oat, pea, sorghum, soybean, and wheat) in north-central USA using principal component regressions. For the part of the study site dominated by corn and soybean (cover fraction > 95%), the first principal component (PC1) explained 78% of yield variance, whereas the part of the study site containing wheat and mixed crops PC1 explained 43% of yield variance. Teubner et al. [13] explored the relationship between the crop and grassland Gross Primary Production (GPP) and VOD data taken from SMOS, ASCAT, and AMSR-E. They showed that changes in VOD are generally consistent with changes in GPP, especially for the C- and X-bands.

Even though VOD data from AMSR-E, SMOS, SMAP, and ASCAT allow crop monitoring, the low spatial resolution of these products (25-km for SMOS, 9-km for SMAP, 12.5-km for ASCAT) is a limitation for crop monitoring and irrigation management in agriculture areas. Up to date, there is no VOD product available at the plot scale. The Sentinel-1A (S-1A) and Sentinel-1B (S-1B) sensors operating in the C-band have observation capacity allowing us to derive VOD at plot scale as these instruments provide images with a good revisit time (6 days over Europe) and a high spatial resolution (10 m × 10 m).

The aim of this study is to present a new approach for cropland VOD mapping at plot scale from S-1A and S-1B SAR data. The derivation of VOD is based on the use of the Water Cloud Model (WCM) [19]. The study was conducted over an area of 50 km × 50 km located in Catalonia, Spain, which contains a large variety of crop types. For this area, plot VOD values were derived from S1A and S1B SAR data for two crop growth cycles. The first crop growth cycle is between September 2017

and September 2018 and the second one is between September 2018 and September 2019. The NDVI derived from Sentinel-2 images corrected for atmospheric effects was used to evaluate the robustness of the derived VOD values. Section 2 presents the study area and the data used. Section 3 gives an overview of the methodology. The results are described in Section 4. Section 5 provides a discussion of the results. Finally, Section 6 presents the main conclusions.

2. Study Area and Database

2.1. Study Area

The study was conducted over an area of 50 km by 50 km (altitude between 200 and 900 m), located in Catalonia, Spain (centered on 1.195°E and 41.665°N, as shown in Figure 1). The climate is typically Mediterranean: The mean daily air temperature varies between 4 °C and 28 °C and the average annual precipitation is around 376 mm (347 mm in 2015, 385 mm in 2016, and 397 mm in 2017) (Figure 2) [20]. The zone of this study contains several crops types, for a total of 87439 plots, with plot slopes lower than 10%. Plot delineations and crop types were provided by the Geographical Information System for Agricultural Parcels (http://agricultura.gencat.cat/ca/serveis/cartografia-sig/aplicatius-tematics-geoinformacio/sigpac/descarregues/). The dominant crops are barley (37817 plots), wheat (21562 plots), fallow (5781 plots), corn (5156 plots), bean (3604), alfalfa (3244), oat (1730), and rapeseed (1626). These crops represent 96% of cultivated fields in the study area. The slopes of plots are lower than 10%. A total of 235 Sentinel-1 (S1) images in ascending and descending modes, as well as 24 Sentinel-2 (S2) images acquired between September 2017 and September 2019, were used in this study.

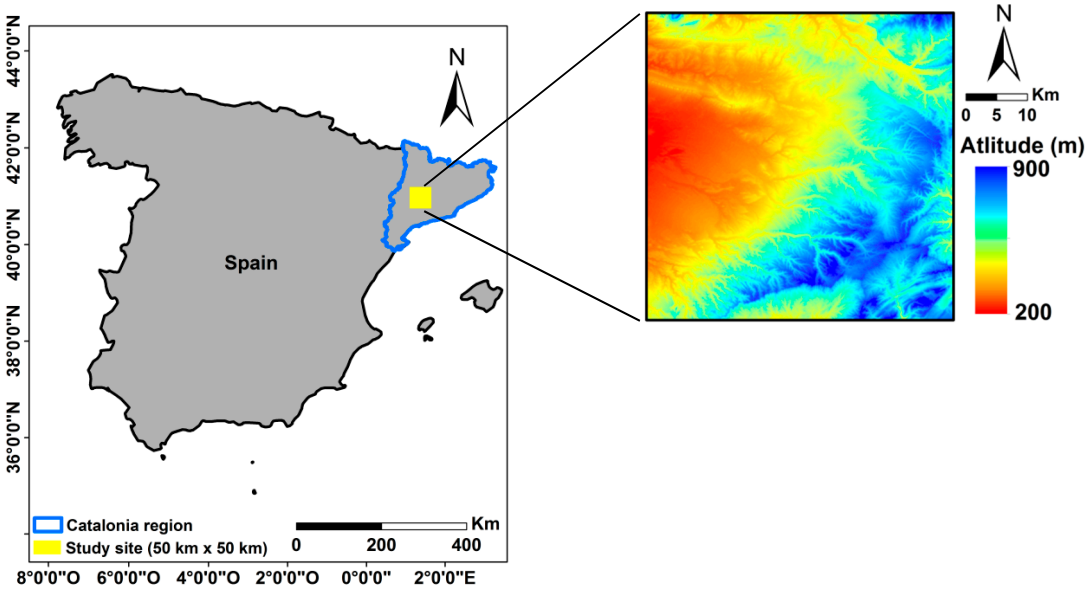

Figure 1. Study site in yellow.

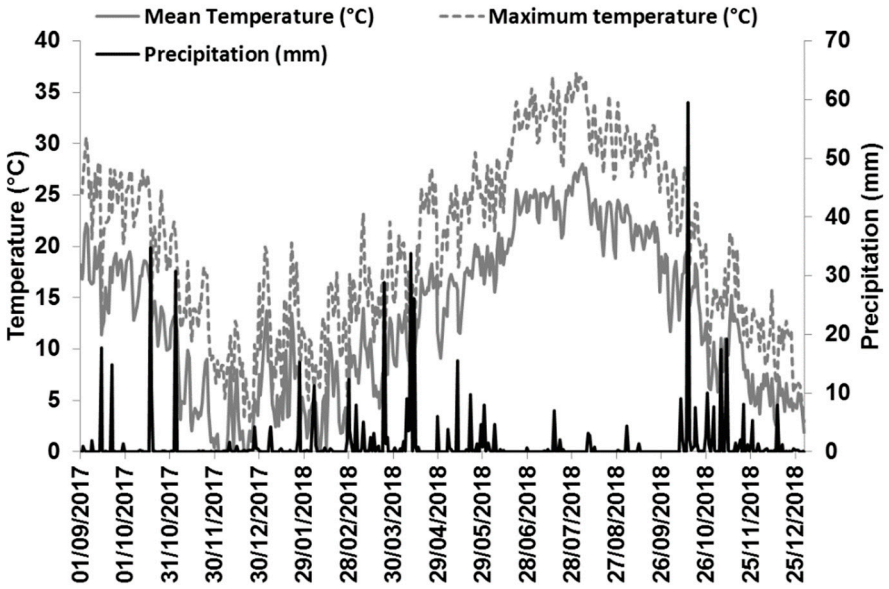

Figure 2. Precipitation (mm) and mean temperature (°C) registered from a weather station in the study zone.

2.2. Database Description

2.2.1. Sentinel-1 Data

In this study, 235 C-band (5.405 Ghz) SAR images acquired by S-1A (launched on 3 April 2014) and S-1B (launched on 25 April 2016) in both ascending (117 images) and descending (118 images) modes were used. These images were acquired between September 2017 and September 2019. The acquisition mode of these images was Interferometric Wide (IW) swath (~250 km × ~150 km) with VV and VH polarizations. The IW swath is the primary conflict-free acquisition mode used over land. The 235 S1 images are derived from the Level-1 Ground Range Detected (GRD) product with a spatial resolution of 10 m × 10 m and a revisit time of 6 days. These images were downloaded from the Copernicus website (https://scihub.copernicus.eu/dhus/#/home, last access September 2019).

The Sentinel-1 toolbox (S1TBX) developed by the European Spatial Agency (ESA) was used to calibrate the S1 images. This calibration converts the digital number of downloaded SAR images to backscattering coefficients in linear unit.

2.2.2. Sentinel-2 Images

In this study, 24 cloud-free S2 images acquired between September 2017 and September 2019 were used (one image each month). The S2 images were obtained from the Theia website at the French Land Data Center (https://www.theia-land.fr/, last access September 2019). Theia provides S2 images corrected for atmospheric effects using the method developed by Hagolle et al. [21,22]. The S2 data were used to generate NDVI images.

3. Methodology

In this study, VOD was computed for two crop growth cycles that occurred between September 2017 and September 2019. VOD computation was based on the use of C-band Sentinel-1 time series and the Water Cloud Model (WCM) [19]. In the WCM, the total backscattered signal (σ^0_{tot}) is the sum of vegetation contribution (σ^0_{veg}) and soil contribution (σ^0_{soil}) attenuated by the vegetation canopy (Equations (1) and (2)). In addition to sensor parameters (SAR wavelength, incidence angle and polarization), soil contribution is a function of soil moisture and surface roughness. WCM does not

consider high order scattering mechanisms like double scattering from ground–stem interactions. The total backscatter, in the power domain, is expressed as follows:

$$\sigma^0_{tot} = \sigma^0_{veg} + T^2\sigma^0_{soil} \quad (1)$$

$$T^2 = e^{-2\frac{VOD}{\cos\theta}} \quad (2)$$

where, θ is the SAR incidence angle (in degrees), and T^2 is the two-way attenuation.

Using two SAR images acquired at two different dates (t_1 and t_2) and by supposing that the vegetation characteristics are constant between these two dates (i.e., $\Delta\sigma^0_{veg,t2-t1} = \sigma^0_{veg,t2} - \sigma^0_{veg,t1} = 0$), Equations (1) and (2) can be solved to estimate VOD as:

$$VOD = -\frac{\cos\theta}{2}\ln\left(\frac{\Delta\sigma^0_{tot,t2-t1}}{\Delta\sigma^0_{soil,t2-t1}}\right) \quad (3)$$

For a given plot, VOD can be analytically computed from Equation (3) if σ^0_{tot} and σ^0_{soil} are known from the SAR images on dates t_1 and t_2. However, to compute σ^0_{soil} from radar backscattering models (e.g., [23–25]), estimates of soil moisture and surface roughness values are needed. These values are often unavailable or available only for a few plots within the study area. It is worth mentioning that VOD estimation from WCM (Equation (3)) may be inaccurate in the case of important double-scattering mechanisms as this mechanism is not considered in Equation (1) as mentioned above.

To estimate VOD over vegetated plots, σ^0_{tot} is computed for a given plot as the average of the SAR pixel values within that plot. Only plots with NDVI values higher than 0.3 are considered for VOD computation in order to ensure that VOD will be computed only over plots covered by vegetation. To compute soil contribution (σ^0_{soil}), we assume that the underlying soil of a given vegetated plot has the same properties (soil moisture and roughness) as the soil of the bare agricultural plots situated in a grid of 5 km × 5 km centered at the considered plot. Bare agricultural soils within SAR images can be spotted using NDVI images calculated from S2 acquisitions. It is assumed that bare soils correspond to NDVI values lower than 0.3 [26,27]. Thus, σ^0_{soil} for a given plot at a given date corresponds to σ^0_{soil} averaged over all S1 bare pixels located in the 5 km × 5 km grid at the same date. This assumption is valid only for non-irrigated plots where the increase and decrease in soil moisture is mainly related to rainfall and temperature conditions which are assumed to be homogeneous in a grid of 5 km × 5 km. For this reason, VOD was computed only for non-irrigated crops (winter crops) in the present study.

VOD values were computed separately from SAR data time series in ascending and descending modes. For each acquisition mode, one VOD value is computed for each set of four consecutive SAR images. The use of four SAR dates to compute one mean VOD value was considered to decrease the noise in VOD computation (we assumed that VOD remains stable during 18 days using four S1 SAR images with a revisit time of 6 days over Europe). This assumption is made in many studies considering VOD retrievals from space-borne observations [28,29].

For each SAR acquisition mode, each combination of two S1 images among the four S1 images (six combinations) was used to compute one VOD value (Equation (3)). This step can generate six possible VOD values (VOD_1, … , VOD_6) for each SAR acquisition mode. Negative VOD values were eliminated, as well as VOD values when both $\Delta\sigma^0_{tot}$ and $\Delta\sigma^0_{soil}$ were lower than 0.5 dB. Indeed, a variation in σ^0_{tot} and σ^0_{soil} lower than 0.5 dB is assumed not to be significant and could be related to SAR radiometric noise. As a result, six VOD values from the four images in ascending mode (VOD_{1A}, … , VOD_{6A}) and six VOD values from the four images in descending mode (VOD_{1D}, … , VOD_{6D}) can be obtained at most for each plot. Finally, for each SAR acquisition mode, the mean of the six VOD values was calculated.

It should be noted that VOD was computed using SAR images in VV and VH polarizations separately. In the following, VOD-VV_A and VOD-VV_D will denote VOD values computed from VV polarization of SAR data in ascending and descending modes, respectively. Similarly, VOD-VH_A and

VOD-VH_D will denote VOD values computed from VH polarization of SAR data in ascending and descending modes, respectively.

To assess the relevance of VOD estimates, the temporal evolution of VOD was analyzed in comparison to that of NDVI for the two crop growth cycles. Several studies have used vegetation indices derived from optical images to evaluate the relevance of VOD estimations over crops since optical indices are well-suited/efficient to monitor the crop development [9,13]. For each polarization and each SAR overpass mode (Ascending and Descending), VOD values obtained over each crop plot were separately averaged for each non-irrigated crop type (barely, fallow, oat, rapeseed, and wheat) and the associated standard deviation (σ) is also calculated. For each crop type, the averaged value of VOD-VV_A, VOD-VV_D, VOD-VH_A, and VOD-VH_D are denoted later as VOD-$VV_{A,av}$, VOD-$VV_{D,av}$, VOD-$VH_{A,av}$, and VOD-$VH_{D,av}$, respectively. Similarly, for each crop type, NDVI values of plots were averaged for the study zone ($NDVI_{av}$). As a reminder, in this study VOD was computed only for non-irrigated crops (winter crops).

4. Results

4.1. VOD Computed using SAR Data in VV Polarization

Figure 3 shows that, in general, VOD-VV values (VOD-$VV_{A,av}$ and $VOD_{D,av}$) in both crop growth cycles have similar temporal dynamics as $NDVI_{av}$. For the first crop growth cycle (between September 2017 and September 2018), VOD-VV values of barley, fallow, oat, and wheat, at the early growth stage (before 1 January 2018) are low (about 0.15) and the $NDVI_{av}$ values are lower than 0.2 (Figure 3a–d). Later, between 1 January 2018 and 1 May 2018, VOD-VV and $NDVI_{av}$ values appear to start increasing at the same time. VOD-VV values reach a maximum values of about 0.50 while $NDVI_{av}$ reach values of about 0.8 in the case of barley, oat, and wheat. In the case of fallow, VOD values reach a maximum of about 0.38 while $NDVI_{av}$ reaches values of about 0.43. Between 1 May 2018 and 1 November 2018, $VOD_{A,av}$ and $VOD_{D,av}$ start decreasing to reach a minimum of ~0.15 while $NDVI_{av}$ reaches about 0.2. Similar results were obtained for the second crop growth cycle (between September 2018 and September 2019) where the temporal dynamics of VOD-VV match well to that of $NDVI_{av}$. However, for the second crop cycle of fallow, two VOD-VV peaks were observed. The first VOD-VV peak is on 25 February 2019 and the second one is on 1 May 2019. An analysis of plots fallow NDVI profiles shows that some plots have high NDVI between December 2018 and February 2019 while the remaining plots have high NDVI between May 2019 and June 2019.

In contrast to the other crop types, Rapeseed VOD-VV values from 1 January 2018 to 1 May 2018 in both growth cycles are not consistent with NDVI (Figure 3e). VOD values are found to be almost constant and do not increase with $NDVI_{av}$ during the growing period. For instance, in the first crop growth cycle, VOD-VV of Rapeseed increases from around 0.15 to 0.20 while $NDVI_{av}$ increases from 0.18 to 0.70.

Moreover, Figure 3 reveals two interesting phenomena observed in both crop growth cycles:

- First, VOD-$VV_{A,av}$ and VOD-$VV_{D,av}$ have very close values except during mainly the periods from 13 May 2018 to 18 June 2018 and from 1 May 2019 to 1 June 2019. During these periods, VOD-$VV_{A,av}$ values are lower than those of VOD-$VV_{D,av}$. For instance, for wheat at around 31 May 2018 (VOD was calculated with S1 images acquired between 13 May 2018 and 31 May 2018), VOD-$VV_{A,av}$ is lower than $VOD_{D,av}$ by 0.18.
- Second, in both crop growth cycles, VOD-$VV_{A,av}$ and VOD-$VV_{D,av}$ reached a peak earlier than NDVI by about 18 days. For instance, for wheat, VOD-$VV_{A,av}$ peaks on 25 April 2018 (VOD calculated with S1 images acquired between 7 April 2018 and 25 April 2018) while the $NDVI_{av}$ peaks on 15 May 2018, about 3 weeks later.

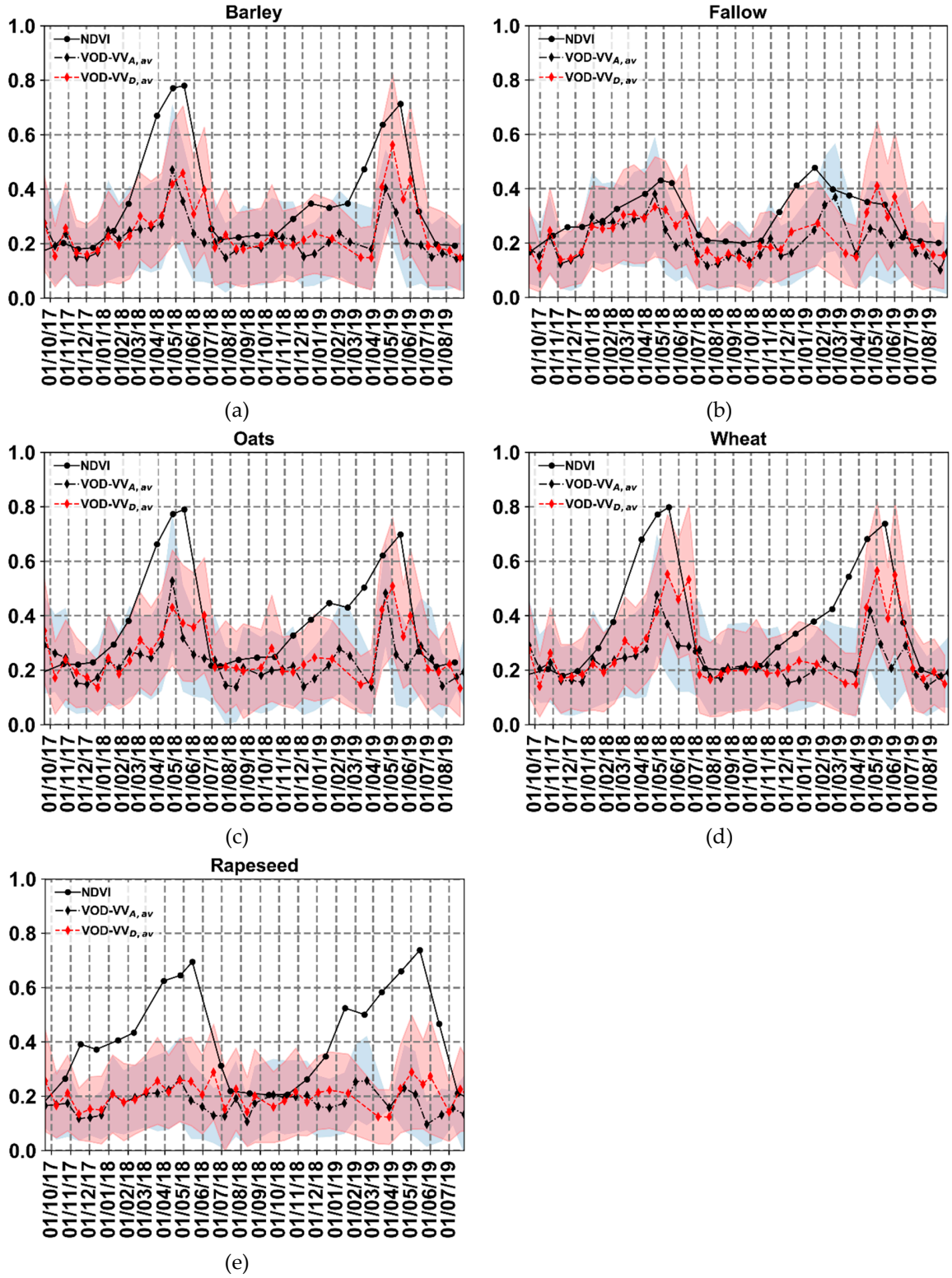

Figure 3. Temporal patterns of VOD values computed at VV polarization (VOD-VV$_A$,av and VOD-VV$_D$,av) and NDVIav. (**a**) Barley, (**b**) Fallow, (**c**) Oat, (**d**) Wheat, (**e**) Rapeseed. The shaded region represents the mean ± standard deviation of VOD values for all plots at a given date.

To better analyze the temporal correlation between the retrieved VOD and NDVI values for both growth cycles, the coefficient of determination between VOD-VV values and NDVI$_{av}$ was computed (Figure 4). For barley, fallow, oat, and wheat, medium to good correlations were obtained (R^2 values

about 0.58, 0.39, 0.46, and 0.61, respectively) (Figure 4a–d). For rapeseed, a poor correlation was obtained (R^2 about 0.18).

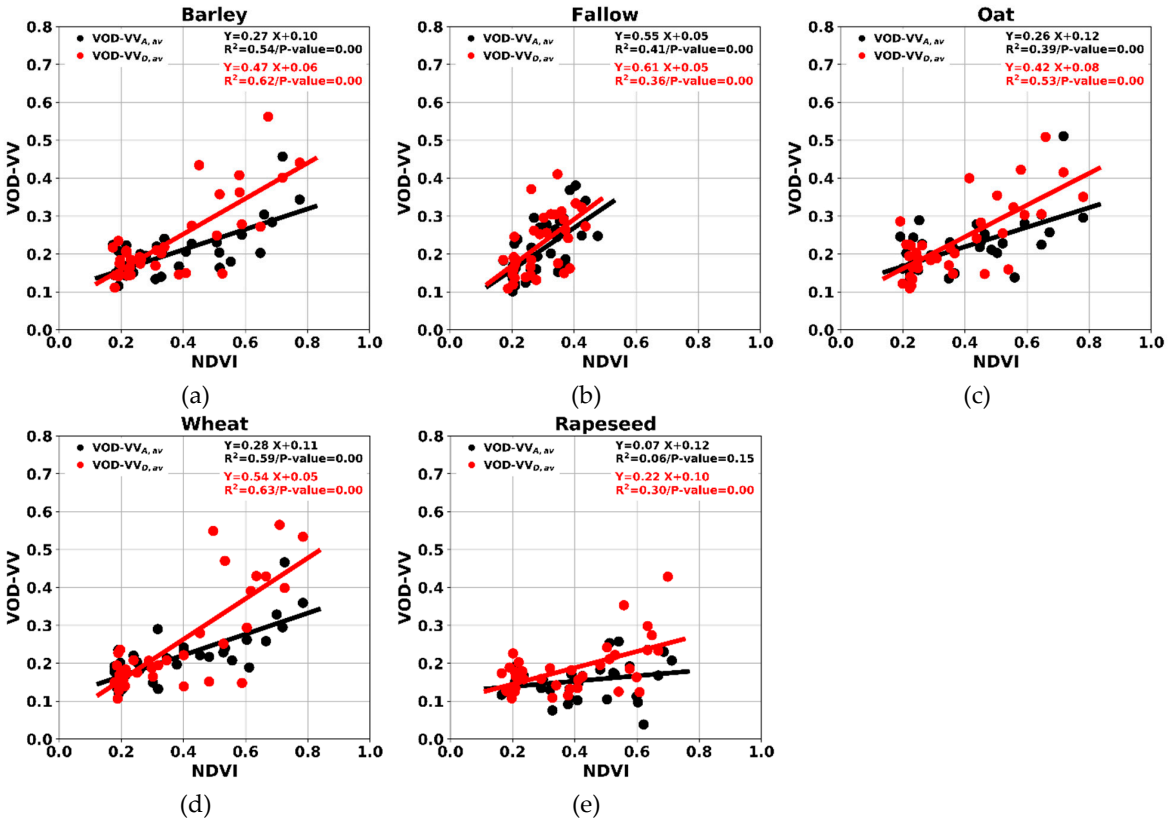

Figure 4. VOD values computed at VV polarization (VOD-$VV_{A,av}$ and VOD-$VV_{D,av}$) as a function of $NDVI_{av}$ values. (**a**) Barley, (**b**) Fallow, (**c**) Oat, (**d**) Wheat, (**e**) Rapeseed.

4.2. VOD Computed using SAR Data in VH Polarization

In this section, the time variations of VOD-VH values (VOD-$VH_{A,av}$, and VOD-$VH_{D,av}$) obtained for the VH polarization are compared to that of $NDVI_{av}$. Figure 5 shows that the temporal dynamic of VOD-VH in both crop growth cycles does not match that of $NDVI_{av}$. During the growing period, VOD-VH values increase slightly (by about 0.10) while $NDVI_{av}$ presents a sharp increase before reaching its peak value. For instance, VOD-$VH_{A,av}$ for wheat increases from 0.16 to 0.27 while $NDVI_{av}$ increases from 0.2 to 0.8 (Figure 6d). Finally, the coefficient of determination (R^2) between VOD-VH and $NDVI_{av}$ is about 0.45 for barely, 0.20 for fallow, 0.26 for oats, 0.40 for wheat, and 0.01 for rapeseed (Figure 6).

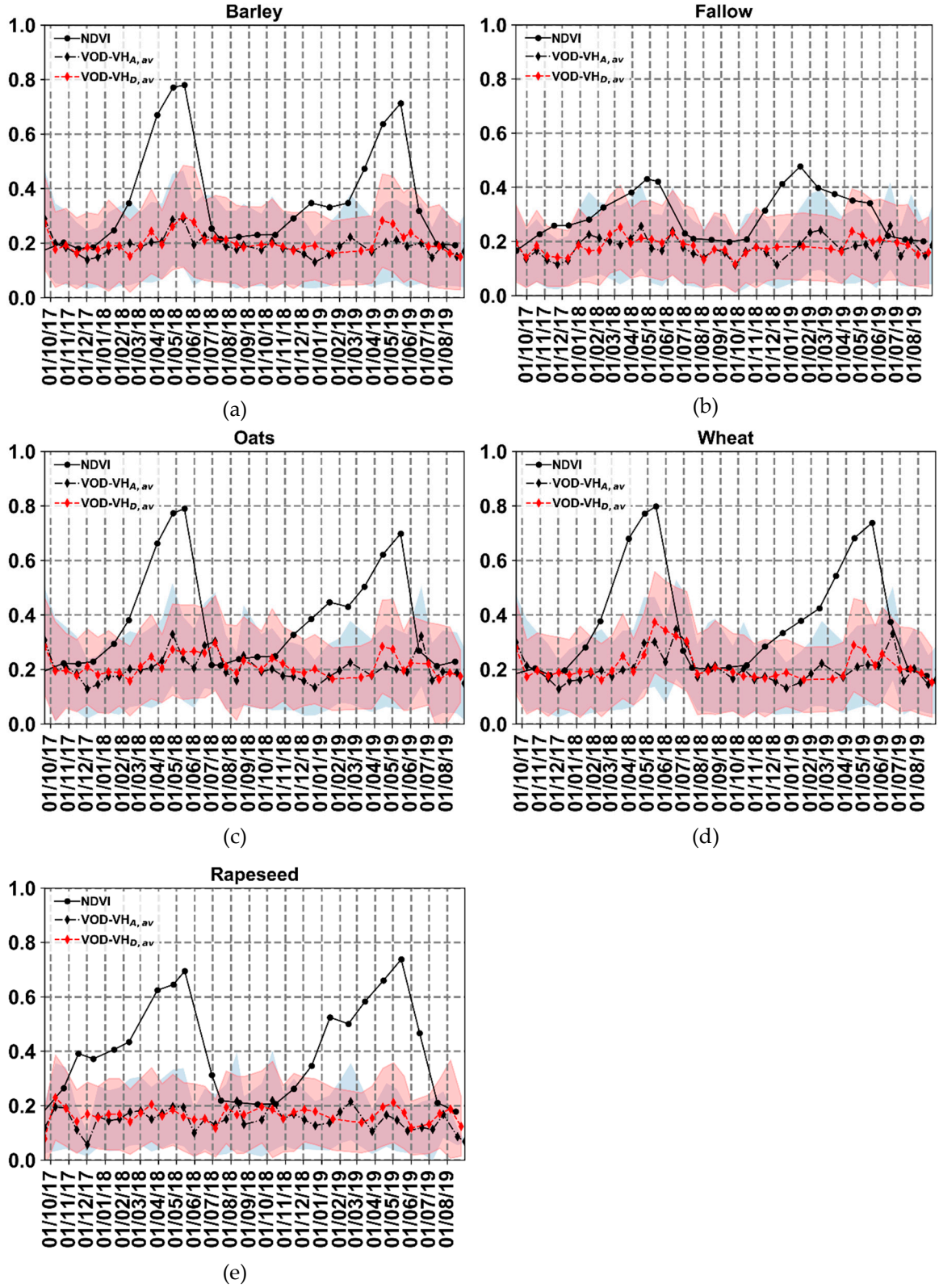

Figure 5. Temporal patterns of VOD values computed from VH polarization (VOD-VH$_{A,av}$ and VOD-VH$_{D,av}$) and NDVI$_{av.}$ (**a**) Barely, (**b**) Fallow, (**c**) Oat, (**d**) Wheat, (**e**) Rapeseed. The shaded region represents the mean ± standard deviation of VOD values for all plots at a given date.

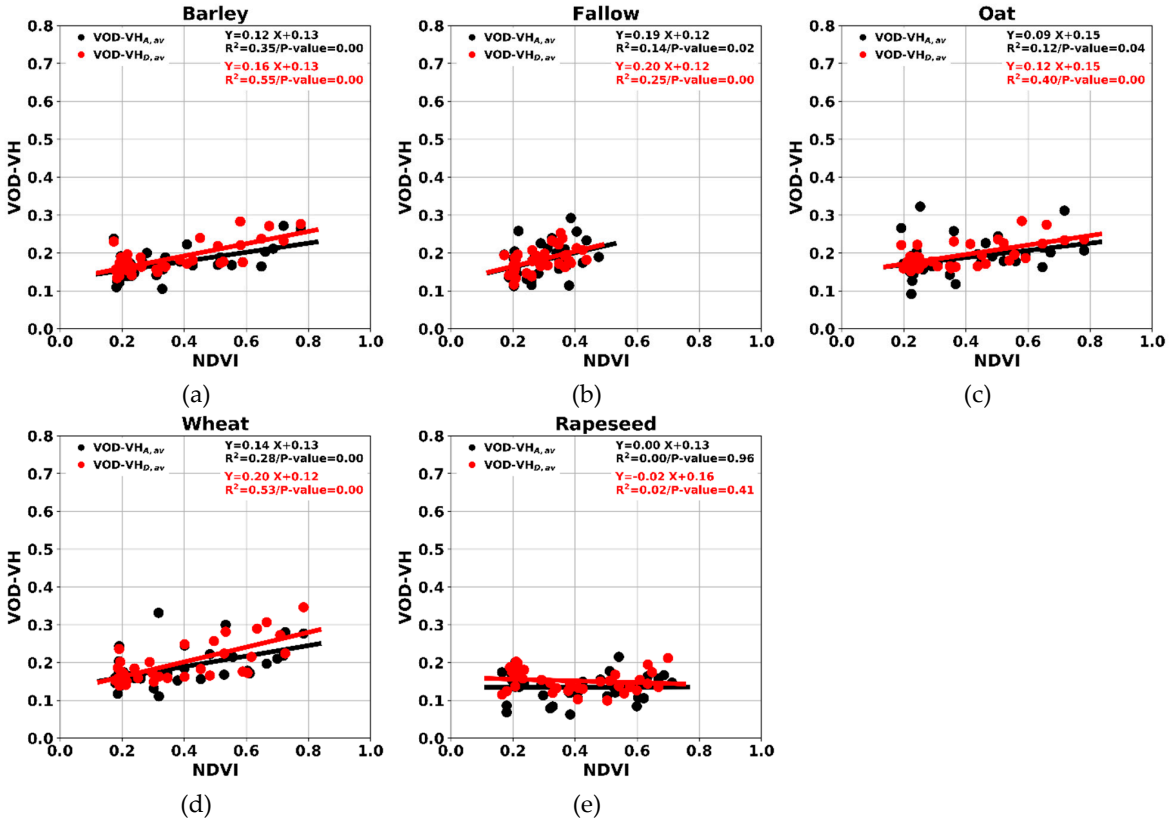

Figure 6. VOD values computed from VH polarization (VOD-VH$_{A,av}$ and VOD-VH$_{D,av}$) as a function of NDVI$_{av}$ values. (**a**) Barley, (**b**) Fallow, (**c**) Oat, (**d**) Wheat, (**e**) Rapeseed.

4.3. Can Vegetation Water Status Maps be Produced using VOD?

The method developed in this study for VOD mapping at plot scale has the potential to become operational since it only uses free and open access S2 and S1 data. VOD maps at plot scale were computed for barley, fallow, oat, and wheat plots located in our study zone, but rapeseed plots were excluded in this mapping process. Each VOD map was obtained using four SAR images (18 days), and the attributed date to each VOD map was that of the last used SAR image, as explained in the method section.

Figure 7 shows four VOD-VV maps with assigned dates 12 February 2018, 2 March 2018, 7 April 2018, 25 April 2018, and 13 May 2018 (Figure 7a–e). Figure 7 also shows NDVI maps for dates close to those assigned to VOD maps (Figure 7f–j). For most plots, VOD values are lower than 0.3 on 12 February 2018 and 2 March 2018 (Figure 7a,b). On 7 April 2018 (Figure 7c), we can observe a spatial heterogeneity in VOD values. The study area appears to be divided into two zones of VOD values. The first zone at the East (delineated by a black polygon) is dominated by VOD values mostly lower than 0.3, while the other zone at the West (delineated by a red polygon) is dominated by higher VOD values (mostly between 0.3 and 0.5). This spatial heterogeneity is more pronounced on 25 April 2018 (Figure 7d) where many plots have high VOD values between 0.5 and 0.8 (mainly plots displayed in orange and red color codes), while small areas in the eastern part of the study area present low to medium VOD values (mainly plots situated in the black dashed ellipsoid). In the VOD map on 13 May 2018, most of the plots with high VOD values on 25 April 2018 present a decrease in VOD to attain low to medium VOD values whereas the majority of the plots with low to medium VOD values on 25 April 2018 present larger VOD values on 13 May 2018 (Figure 7d,e). One possible explanation is that crops with high VOD values on 25 April 2018 were sown before those with low VOD values and have reached a more advanced stage in the growth cycle.

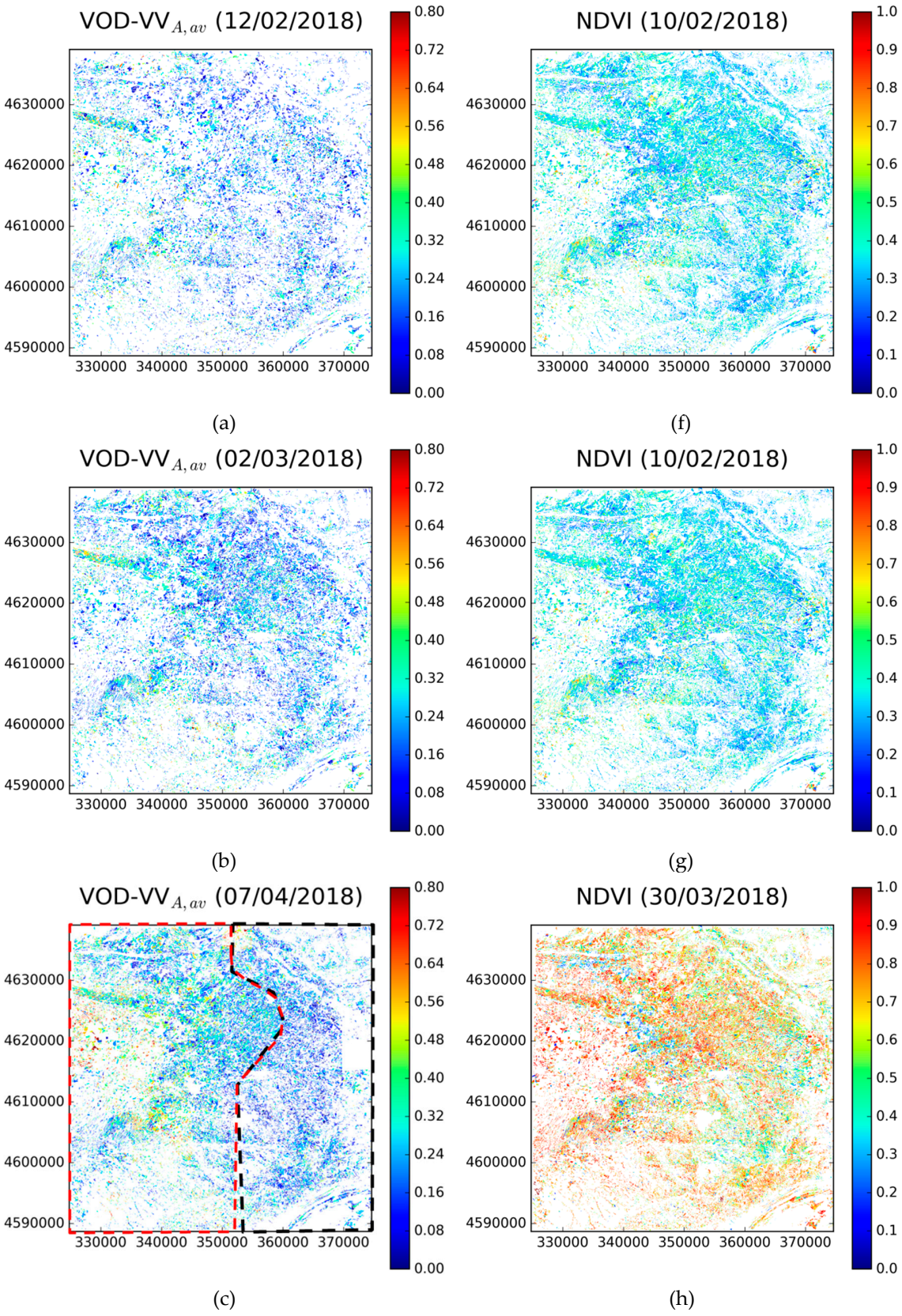

Figure 7. *Cont.*

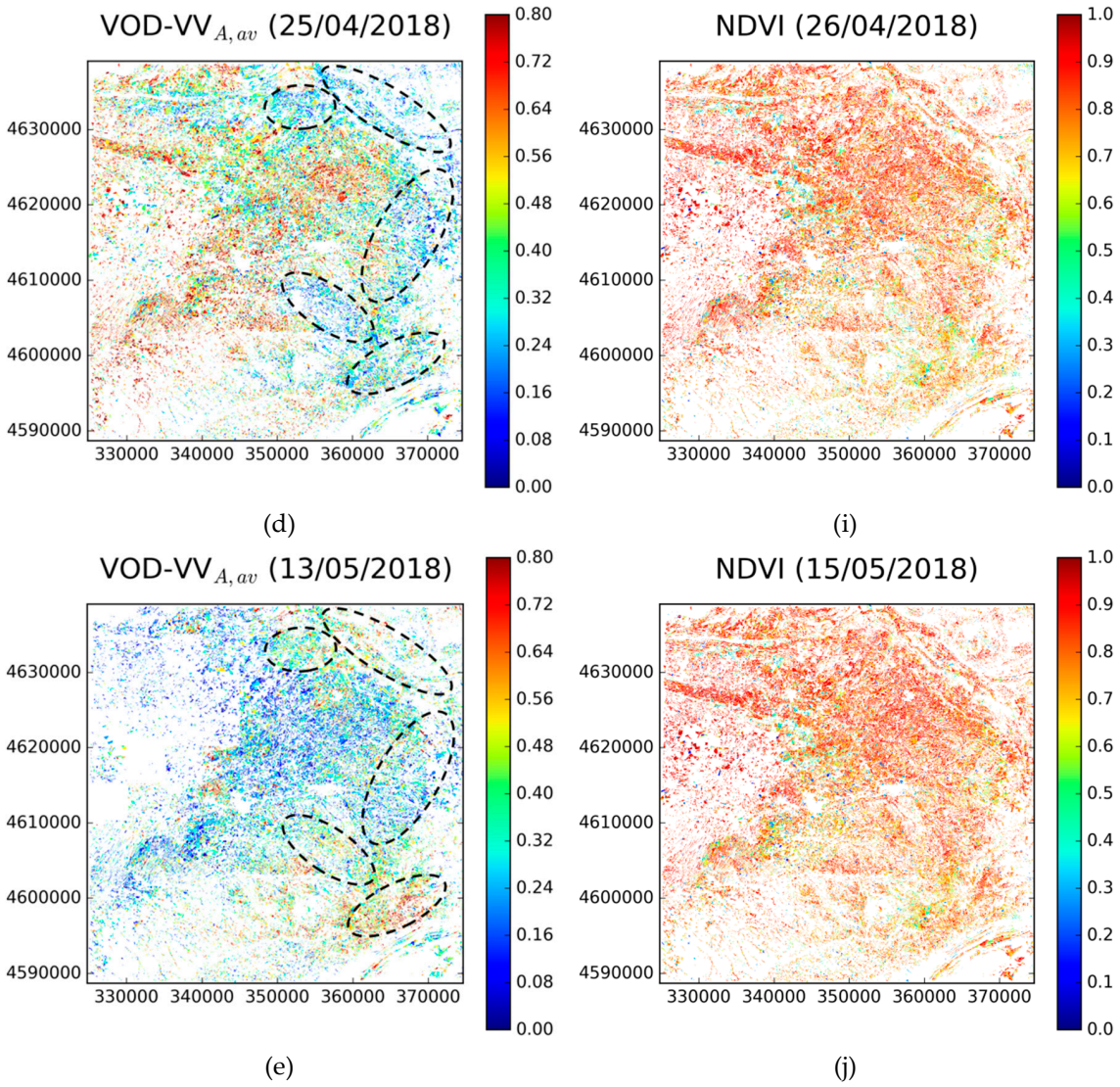

Figure 7. Maps of VOD derived from S1 images at VV polarization in Ascending mode for the dates of 12/02/2018 (**a**), 02/03/2018 (**b**), 07/04/2018 (**c**), 25/04/2018 (**d**), and 13/05/2018 (**e**). In addition, maps of NDVI for the dates of 10/02/2018 (**f**,**g**), 30/03/2018 (**h**), 26/04/2018 (**i**), and 15/05/2018 (**j**). Coordinates are in UTM (Universal Transverse Mercator) ZONE 31 North.

Finally, results show that between 12 February 2018 and 25 April 2018 VOD-VV values tend to increase together with NDVI. However, VOD-VV (Ascending, 18h00) starts to decrease on 13 May 2018 while NDVI values remain high (Figure 7e,j). This was expected since VOD peaked earlier than NDVI (Figure 3).

5. Discussion

5.1. Impact of Our Assumption of Spatial Homogeneity of Soil Moisture and Roughness on VOD Calculation

5.1.1. Impact of Soil Moisture Spatial Homogeneity

In this study, it is assumed that the surface soil moisture (SSM) for vegetated plots is similar to the averaged SSM of all bare soils in the surrounding 5 km × 5 km. However, in some places the SSM is not homogeneous in a pixel of 5 km × 5 km due to many factors related, and not limited to, meteorological context and soil texture. In-situ SSM measurements performed between 2016 and 2018 over non-irrigated plots (mainly non-irrigated wheat and grassland), located in a flat area with

dimension of 15 km × 15 km around Montpellier region of France, were analyzed. Within this area, the SSM values of plots with vegetation cover were close to the averaged SSM values of all bare plots in the 15 km × 15 km area. The histogram displayed in Figure 8 (established using 165 samples) shows the distribution of the difference between the SSM of each vegetated plot (Height > 15 cm) and the averaged SSM of all bare plots (vegetation height < 15 cm). The mean of the difference distribution is about 1.1 vol.% with a standard deviation (std) of 3.0 vol.%. This result signifies that the SSM values of non-irrigated plots (bare or with vegetation cover) were homogeneous (up to a certain limit) within the area of 15 km × 15 km. However, even though most in-situ SSM points show a high consistency between the SSM measured on plots with vegetation cover and the average SSM calculated using all the SSM measurements made on the bare soil plots in an area of 15 km × 15 km, Figure 8 also shows that for a small part of the data, the SSM of plots with vegetation are 5 vol.% higher than the SSM of the bare soils.

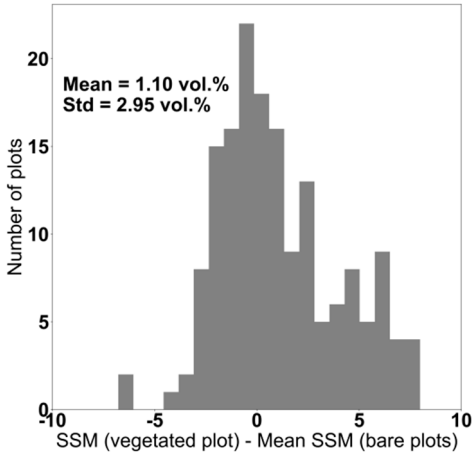

Figure 8. Difference between the SSM measured in each vegetated plot (vegetation height > 15 cm) and the averaged SSM of all bare plots (vegetation height < 15 cm) in an area of 15 km × 15 km.

Furthermore, a sensitivity analysis was performed to assess the impact of 5 vol.% SSM underestimation for vegetated soil on VOD estimation from Equation (3). Indeed, we assume in our method that the SSM of vegetated plots is similar to that of bare soils whereas in fact the SSM of vegetated plots could be in some cases higher than the SSM of bare soils (about 5 vol.% as shown in Figure 8). First, the impact of the error on the SAR backscattering coefficients σ^0_{tot} and σ^0_{soil} due to an 5 vol.% underestimation for the SSM of vegetated plots is quantified. Then, the impact of the errors on σ^0_{tot} and σ^0_{soil} on VOD estimation was investigated through sensitivity analysis of Equation (3).

A synthetic database of σ^0_{soil} and of σ^0_{tot} was generated using the calibrated IEM combined with the Water Cloud Model [23,30] for SSM values between 10 and 30 vol.% (step of 5 vol.%), NDVI between 0.4 and 0.8, soil roughness defined by the root mean surface height "*Hrms*" fixed to 1.5 cm, and SAR incidence angle "θ" was fixed to 35° (S1 incidence angle). From each reference element of the synthetic database (composed of θ, *Hrms*, SSM and NDVI), 1000 elements containing SSM values noisy with a Gaussian noise with a mean of 5 vol.% and std of 5 vol.% were generated. Using the calibrated Integral Equation Model and the Water Cloud Model, σ^0_{soil} and σ^0_{tot} were computed for each reference element (reference σ^0_{soil} and σ^0_{tot}) and for the corresponding 1000 noisy elements (noisy σ^0_{soil} and σ^0_{tot}). Finally, the noisy σ^0_{soil} and σ^0_{tot} and the corresponding reference σ^0_{soil} and σ^0_{tot} were compared, and the bias (noisy σ^0_{soil} minus the reference σ^0_{soil}, and noisy σ^0_{tot} minus the reference σ^0_{tot}) as well as the Root Mean Square Error (RMSE) on σ^0_{soil} and σ^0_{tot} were computed. Results showed that an underestimation of the vegetated plots SSM by 5 vol.% induces an error on σ^0_{soil} by 0.85 dB for the bias and 1.43 dB for the RMSE. Concerning the error on σ^0_{tot}, a bias of 0.63 dB and an RMSE of 0.99 dB were observed.

Next, a sensitivity analysis was performed to assess the impact of these errors of σ^0_{soil} and σ^0_{tot} on VOD values computed from Equation (3). For each possible couple of reference elements

(σ^0_{soil} and σ^0_{tot}) and their associated noisy elements, reference VOD and noisy VOD were computed. Then, the reference VOD values (without error on SSM) and noisy VOD values were compared (Figure 9). Results show that an underestimation of the vegetated plots SSM of 5 vol.% leads to a slight underestimation of VOD of 0.02 (with an RMSE of 0.04). In addition, the impact of 5 vol.% SSM underestimation on VOD estimations was analyzed according to the NDVI for values between 0.4 and 0.8 (Figure 10). The underestimation of VOD as well as the RMSE increases when the NDVI increases. The underestimation on VOD increases from 0.010 for NDVI = 0.4 to 0.035 for NDVI=0.8. Similarly, the RMSE increases from 0.02 for NDVI=0.4 to 0.06 for NDVI=0.8. Accordingly, the assumption about the equivalence between σ^0_{soil} of vegetated plots and that of bare plots in the surrounding 5 km × 5km considered in order to solve the Equation (3) would not considerably impact VOD estimation.

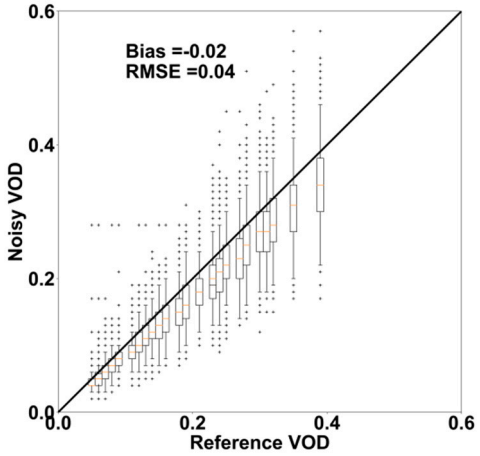

Figure 9. Impact of 5 vol.% vegetated plots SSM underestimation on VOD estimations: Noisy VOD as a function of reference VOD.

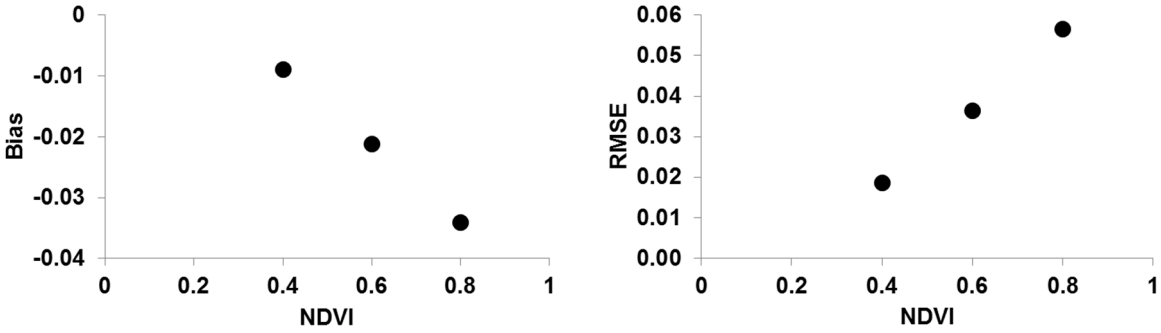

Figure 10. Impact of 5 vol.% vegetated plots SSM underestimation on VOD estimations: Bias (noisy VOD—reference VOD) and RMSE are plotted as a function of NDVI.

5.1.2. Impact of Soil Roughness Spatial Homogeneity

A wide in-situ surface soil roughness dataset (defined by the root mean square surface height *Hrms*), collected over several agricultural study sites [24,30], was used to analyze the distribution of *Hrms* values in agricultural areas (around 500 samples). Measurements of soil roughness were carried out using a needle profilometer 1 m in length with 2 cm sampling intervals. Ten roughness profiles were established in each plot. From these profiles, two surface roughness parameters were then calculated: the average root mean square surface height (*Hrms*), which specifies the vertical scale of the roughness, and the correlation length (*L*), representing the horizontal scale. In general, the *Hrms*-values of cultivated winter crops (wheat, barley, oat, rapeseed . . .) are between 1 and 1.5 cm, whereas they fall between 1 and 3 cm for 90% of the measurements carried out on agricultural bare plots (Figure 11).

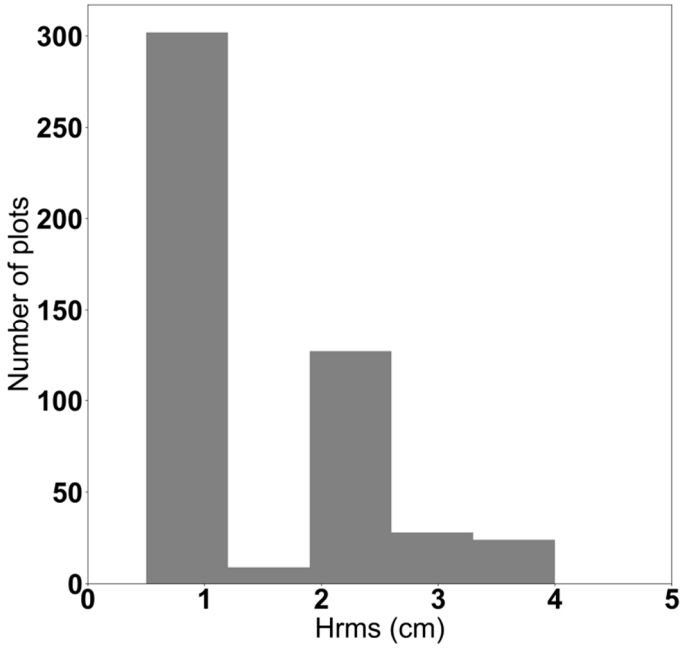

Figure 11. Distribution of *Hrms* values measured over several agricultural plots in several study sites.

In the present study, it was assumed that the *Hrms* for all agricultural plots located within an area of 5 km × 5 km is similar. However, in some places the *Hrms* values are not homogeneous in an area of 5 km × 5 km because some plots are plowed (in general, higher *Hrms*) and others are cultivated (in general, lower *Hrms*). Thus, in some cases, the *Hrms* of plots with vegetation cover may be lower than the averaged *Hrms* over an area of 5 km × 5 km.

An analysis on the impact of this overestimation of *Hrms* on the calculation of VOD was carried out by using the calibrated Integral Equation Model combined with the Water Cloud Model [23,30]. The C-band radar signal was simulated as a function of *Hrms* for a θ of 35° (S1 incidence angle) and a SSM of 20 vol.% (Figure 12). Results show that an overestimation of *Hrms* by about 1 cm on average for the plots with vegetation cover (assuming that *Hrms* of plots with vegetation = average *Hrms* of bare soils) would lead to an overestimation of the soil contribution of 1 dB maximum (Figure 12).

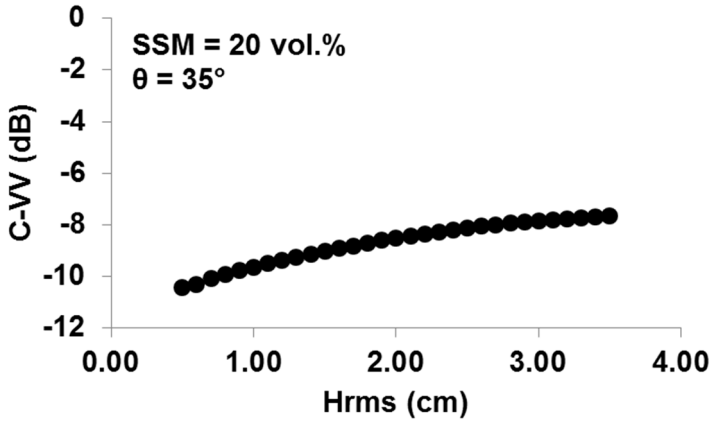

Figure 12. Behavior of radar signal according to *Hrms* using C-band, θ of 35°, SSM of 20 vol.% and VV polarization. The calibrated Integral Equation Model was used for these simulations.

The impact of a 1 cm *Hrms* overestimation of vegetated plots on VOD estimates was investigated through a sensitivity analysis of Equation (3). As done for analyzing the impact of SSM errors on VOD estimation, a synthetic database of σ^0_{soil} and of σ^0_{tot} was computed using the calibrated IEM combined

with the Water Cloud Model [23,30] for *Hrms* values between 1 and 3.5 cm (step of 0.1 cm), NDVI between 0.4 and 0.8, SSM fixed to 20 vol.%, and θ was fixed to 35°. From each reference element of the synthetic database composed of θ, *Hrms*, SSM, and NDVI, 1000 elements containing *Hrms*-values noisy with a Gaussian noise of 1 cm mean and 1 cm standard deviation were generated.

Figure 13 shows the reference VOD values (without bias on *Hrms*) and noisy VOD values (1 cm *Hrms* overestimation). Results show that a 1 cm *Hrms* overestimation leads to a slight overestimation of VOD of 0.03 (with an RMSE of 0.04). In addition, the impact of 1 cm *Hrms* overestimation on VOD estimation was analyzed according to the NDVI for values between 0.4 and 0.8. The overestimation of VOD as well as the RMSE increase as the NDVI increases (Figure 14). The overestimation on VOD increases from 0.02 for NDVI = 0.4 to 0.05 for NDVI = 0.8. Similarly, the RMSE increases from 0.02 for NDVI = 0.4 to 0.05 for NDVI = 0.8. Accordingly, the assumption about the equivalence between σ^0_{soil} of vegetated plots and that of bare plots in the surrounding 5 km × 5 km considered in order to solve Equation (3) would not considerably impact VOD estimation.

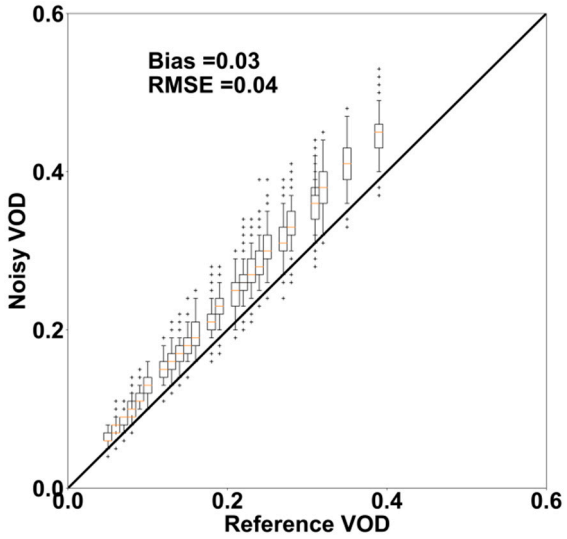

Figure 13. Impact of 1 cm *Hrms* overestimation on VOD estimations: Noisy VOD as a function of reference VOD.

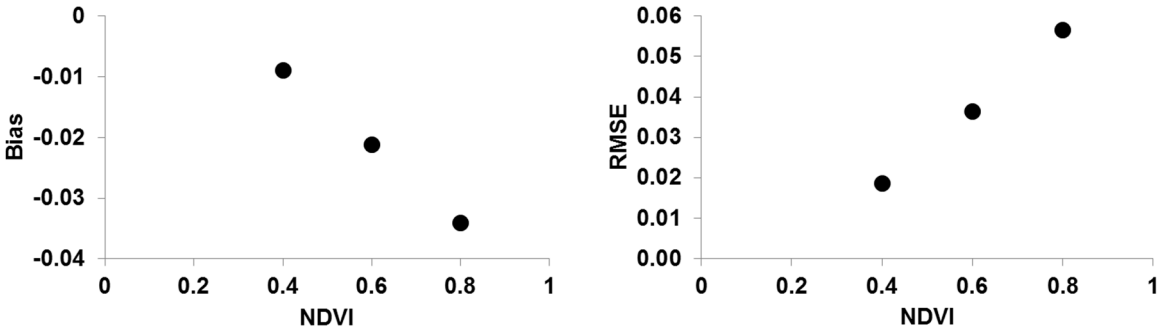

Figure 14. Impact of 1 cm overestimation on VOD estimations: Bias (noisy VOD—reference VOD) and RMSE are plotted as a function of NDVI.

5.2. Complementarity of NDVI and VOD in Vegetation Monitoring

At VV polarization, results show that VOD values obtained from the SAR data in ascending and descending mode fit the temporal dynamics of NDVI (R^2 varies from 0.39 to 0.61 for barley, fallow, oat, and wheat) (Figures 3 and 4). However, these VOD-VV values peak earlier than the NDVI by about 18 days (Figure 3). A possible explanation is that during the beginning of the senescence period (mainly in May for winter crop), the canopy begins to lose water content while photosynthetic activity

has not yet decreased; so that VOD, which is sensitive to the vegetation water content (VWC), begins to decrease while NDVI, which is sensitive to the vegetation photosynthetic activity, continues increasing or remains stable [31,32]. Another possible explanation is that during the growing season the NDVI saturates earlier than VOD (namely, the peak in the vegetation photosynthetic activity cannot be well identified with the NDVI index) and thus the NDVI will decrease later than VOD. The value of 18 days, which represents the difference between NDVI peak date and VOD peak date, may be inaccurate since NDVI data are sometimes missing and the temporal resolution of computed VOD is 18 days. However, according to temporal profiles of NDVI and VOD in both growth cycles, this difference cannot be shorter than 18 days. On the other hand, Jones et al. [33] showed that NDVI reached a peak earlier than VOD computed from ARMS-E. Similarly, Lawrence et al. [10] showed that VOD computed from SMOS (L-band) peaked later than MODIS LAI values, with an estimated time difference of about 19 days. Such inconstancy may be related to the SAR technology and the used frequency. In this study, SAR C-band (5.4 GHz) data were used, whereas in the studies of Jones et al. [33] and Lawrence et al. [10] data used were provided from radiometers at 18.7 GHz and 1.4 GHz, respectively.

Moreover, the use of the SAR data in both ascending and descending modes provides approximately the same VOD values, except for the periods from 13 May 2018 to 18 June 2018 and from 1 May 2019 to 1 June 2019 (Figure 3). During these periods, it is observed that VOD computed from ascending SAR images acquired at the end of the day (~18h00 UTC) is lower than VOD computed from descending SAR images acquired in the morning (~06h00 UTC). This observation may be explained by the fact that VWC is much lower at 18 h than at 6 h due to canopy water loss (stress and/or transpiration) which increases during the day, especially in the presence of high temperatures [7,34]. Indeed, Figure 2 shows that between 3 May 2018 and 18 June 2018, the daily average temperature increased to a ~25 °C (daily maximum temperature varied between 24 °C and 33 °C). This may indicate that VOD-VV derived from S1 has the potential to monitor plants water status at the plot scale. This is consistent with results obtained at a large scale over the USA by Schroeder et al. [35].

At VH polarization, VOD computed separately from S1 images in ascending and descending mode are weakly correlated to NDVI (R^2 varies between 0.1 and 0.5 for barley, fallow, oat, and wheat) (Figures 5 and 6). The VH signal results from the incident wave depolarization caused principally by volume scattering, namely multiple interactions between SAR microwave radiations and vegetation elements [36,37]. Thus, VH observations are more sensitive to the vegetation structure than the vegetation water content [38,39]. Moreover, multiple scattering mechanisms are not taken into account in the simple WCM model formulation. The used WCM describes soil surface scattering attenuated by vegetation canopy, an attenuation parameterized by the vegetation water content.

Finally, in contrast to NDVI, VOD is an all-weather parameter. This property (all-weather parameter) is particularly useful in rainy spring situations. For example, the description of the rainy spring episode of the year 2016 in the Paris region by Ben-Ari et al. [40] was not possible with NDVI and LAI indices because of clouds.

5.3. Possible Limitations of WCM Modelling?

In this study, it is shown that VOD retrievals for rapeseed are probably not logical (not correlated to NDVI). Yang et al. [24] reported that an important double bounce scattering mechanism may occur over a well-developed rapeseed crop after a heavy rainfall. The double bounce scattering could be due to soil moisture increase in the underlying soil and to the presence of water standing in the canopy. The observations of Yang et at. [24] fit particularly well with our case study since between 24 March 2018 and 12 May 2018 and between 1 March 2019 and 1 June 2019, when the rapeseed was well-developed (NDVI between 0.6 and 0.7), frequent rainfall events occurred (Figure 2). Thus, the inaccurate VOD estimation obtained over our study area may be related to the double scattering mechanism which is not considered in the WCM modelling.

In our method we assume that there is no difference in the vegetation contribution to total backscatter between two images up to 18 days apart. However, substantial fresh biomass and structural

changes can occur within 18 days, particularly during the vegetative stages [41,42]. The choice of 18 days is the compromise to have enough images (four S1 images), to robustly estimate VOD while assuming that the vegetation has changed a little. In some cases, this assumption may not be valid. As a reminder, currently, VOD is calculated using only low spatial resolution data but with a revisit time of about 1 day (SMOS, SMAP, and ASCAT). The 1-day revisit time allows combining several data to estimate VOD once a year or once a month.

It is worth mentioning that for the regions in the world where the revisit time of S1 is 12 days (region outside Europe), VOD computed using the present method may be useless for crop monitoring. In the case of 12 days revisit time, the use of four images (as in the present method) will lead to one VOD value each 36 days, which is longer than one crop growth stage's period, and thus the assumption about vegetation condition stability considered in order to resolve Equation (3) will be no longer valid. Finally, the approach developed in this study is not applicable for irrigated plots.

6. Conclusions

In this study, an approach for Vegetation Optical Depth (VOD) mapping at plot scale has been proposed. This approach is based on retrievals from times series of Sentinel-1 (S1) images using the Water Cloud Model (WCM). The approach developed here is valid only for non-irrigated areas. The NDVI derived from Sentinel-2 images was used to evaluate the relevance of our VOD estimations. VOD values were computed separately at VV and VH polarizations and from ascending and descending modes.

For VOD computed at VV polarization, results show that the temporal dynamic of the estimated VOD fits generally well with the temporal dynamics of NDVI. In general, a medium to good correlation between VOD and NDVI temporal dynamics was obtained (R^2 about 0.58, 0.39, 0.46, and 0.61 for barley, fallow, oat, and wheat, respectively). However, during the beginning of the senescence period (from 25/04/2018 to 15/05/2018 and from 20/04/2019 to 10/05/2019), VOD and NDVI values became uncorrelated. VOD started decreasing on 25/04/2018 in the first crop growth cycle and on 20/04/2019 in the second crop cycle due to a decrease in the canopy water content while NDVI continued increasing due to the increase in the vegetation photosynthetic activity. Moreover, results showed that in the presence of a high temperature over a well-developed canopy (NDVI reaching its peak value), VOD values computed from the SAR images acquired at ~18h (Ascending mode) were lower than those computed from the SAR images acquired at ~6h (Descending mode). This observation was attributed to changes in the canopy water status which leads to a decrease in VWC during the hot afternoon. Finally, our results showed that the temporal dynamics of VOD values computed from VH polarization do not perfectly match that of NDVI (R^2 lower than 0.4 for barley, fallow, oat, and wheat). It is likely due to the multiple-scattering mechanisms present in VH polarization and which is not considered in WCM formulation. In future, other more complex modelling approaches will be used to better account for these volume scattering effects.

The developed approach should be applied to other agricultural areas with more crop types to better assess its relevance. Moreover, in a context of operational crop monitoring, future work will focus on improving the approach developed in this study to map VOD over irrigated agricultural areas. Finally, to well assess the relevance of VOD computation, estimated VOD values should be compared to in-situ measurements of VWC [43].

Author Contributions: Conceptualization, M.E.H. and N.B.; Methodology, M.E.H. and N.B.; Validation, J.-P.W., M.Z., C.A., J.-C.C., and I.F.; Formal Analysis, M.E.H. and N.B.; Investigation, M.E.H. and N.B.; Writing-Original Draft Preparation, M.E.H.; Writing-Review & Editing, N.B., J.-P.W., M.Z., C.A., J.-C.C., and I.F.; Supervision, N.B.

Funding: This research was funded by the French Space Study Center (CNES, TOSCA program) and the National Research Institute of Science and Technology for Environment and Agriculture (IRSTEA).

Acknowledgments: The authors wish to thank the French Space Study Center (CNES, TOSCA program) and the National Research Institute of Science and Technology for Environment and Agriculture (IRSTEA) for supporting this work. Moreover, the authors wish to thank the European Spatial Agency (ESA) for the distribution of Sentinel-1 and Sentinel-2 data, and the French land data center (Theia) for providing Sentinel-2 images corrected

for atmospheric effects. Finally, authors wish to thank the General Direction of Rural Development of the Department of Agriculture, Livestock, Fishing and Food of the Generalitat of Catalunya for providing the SIGPAC data and in particular Maria Jose Escorihuela.

Conflicts of Interest: The authors declare no conflict of interest.

References

1. El Hajj, M.; Baghdadi, N.; Cheviron, B.; Belaud, G.; Zribi, M. Integration of remote sensing derived parameters in crop models: Application to the PILOTE model for hay production. *Agric. Water Manag.* **2016**, *176*, 67–79. [CrossRef]
2. Baret, F.; Guyot, G. Potentials and limits of vegetation indices for LAI and APAR assessment. *Remote Sens. Environ.* **1991**, *35*, 161–173. [CrossRef]
3. Baret, F.; Hagolle, O.; Geiger, B.; Bicheron, P.; Miras, B.; Huc, M.; Berthelot, B.; Niño, F.; Weiss, M.; Samain, O. LAI, fAPAR and fCover CYCLOPES global products derived from VEGETATION: Part 1: Principles of the algorithm. *Remote Sens. Environ.* **2007**, *110*, 275–286. [CrossRef]
4. Duchemin, B.; Hadria, R.; Erraki, S.; Boulet, G.; Maisongrande, P.; Chehbouni, A.; Escadafal, R.; Ezzahar, J.; Hoedjes, J.C.B.; Kharrou, M.H. Monitoring wheat phenology and irrigation in Central Morocco: On the use of relationships between evapotranspiration, crops coefficients, leaf area index and remotely-sensed vegetation indices. *Agric. Water Manag.* **2006**, *79*, 1–27. [CrossRef]
5. Weiss, M.; Baret, F.; Smith, G.J.; Jonckheere, I.; Coppin, P. Review of methods for in situ leaf area index (LAI) determination: Part II. Estimation of LAI, errors and sampling. *Agric. For. Meteorol.* **2004**, *121*, 37–53. [CrossRef]
6. Meesters, A.G.; De Jeu, R.A.; Owe, M. Analytical derivation of the vegetation optical depth from the microwave polarization difference index. *IEEE Geosci. Remote Sens. Lett.* **2005**, *2*, 121–123. [CrossRef]
7. Konings, A.G.; Piles, M.; Das, N.; Entekhabi, D. L-band vegetation optical depth and effective scattering albedo estimation from SMAP. *Remote Sens. Environ.* **2017**, *198*, 460–470. [CrossRef]
8. Vreugdenhil, M.; Dorigo, W.A.; Wagner, W.; De Jeu, R.A.; Hahn, S.; Van Marle, M.J. Analyzing the vegetation parameterization in the TU-Wien ASCAT soil moisture retrieval. *IEEE Trans. Geosci. Remote Sens.* **2016**, *54*, 3513–3531. [CrossRef]
9. Pfeil, I.; Vreugdenhil, M.; Hahn, S.; Wagner, W.; Strauss, P.; Blöschl, G. Improving the Seasonal Representation of ASCAT Soil Moisture and Vegetation Dynamics in a Temperate Climate. *Remote Sens.* **2018**, *10*, 1788. [CrossRef]
10. Lawrence, H.; Wigneron, J.-P.; Richaume, P.; Novello, N.; Grant, J.; Mialon, A.; Al Bitar, A.; Merlin, O.; Guyon, D.; Leroux, D. Comparison between SMOS Vegetation Optical Depth products and MODIS vegetation indices over crop zones of the USA. *Remote Sens. Environ.* **2014**, *140*, 396–406. [CrossRef]
11. Wigneron, J.-P.; Kerr, Y.; Waldteufel, P.; Saleh, K.; Escorihuela, M.-J.; Richaume, P.; Ferrazzoli, P.; De Rosnay, P.; Gurney, R.; Calvet, J.-C. L-band microwave emission of the biosphere (L-MEB) model: Description and calibration against experimental data sets over crop fields. *Remote Sens. Environ.* **2007**, *107*, 639–655. [CrossRef]
12. Patton, J.; Hornbuckle, B. Initial validation of SMOS vegetation optical thickness in Iowa. *IEEE Geosci. Remote Sens. Lett.* **2012**, *10*, 647–651. [CrossRef]
13. Teubner, I.E.; Forkel, M.; Jung, M.; Liu, Y.Y.; Miralles, D.G.; Parinussa, R.; van der Schalie, R.; Vreugdenhil, M.; Schwalm, C.R.; Tramontana, G.; et al. Assessing the relationship between microwave vegetation optical depth and gross primary production. *Int. J. Appl. Earth Obs. Geoinform.* **2018**, *65*, 79–91. [CrossRef]
14. Kirdiashev, K.P.; Chukhlantsev, A.A.; Shutko, A.M. Microwave radiation of the earth's surface in the presence of vegetation cover. *Radiotekhnika Elektron.* **1979**, *24*, 256–264.
15. Mo, T.; Choudhury, B.J.; Schmugge, T.J.; Wang, J.R.; Jackson, T.J. A model for microwave emission from vegetation-covered fields. *J. Geophys. Res. Oceans* **1982**, *87*, 11229–11237. [CrossRef]
16. Jackson, T.J.; Schmugge, T.J. Vegetation effects on the microwave emission of soils. *Remote Sens. Environ.* **1991**, *36*, 203–212. [CrossRef]
17. Brandt, M.; Rasmussen, K.; Peñuelas, J.; Tian, F.; Schurgers, G.; Verger, A.; Mertz, O.; Palmer, J.R.; Fensholt, R. Human population growth offsets climate-driven increase in woody vegetation in sub-Saharan Africa. *Nat. Ecol. Evol.* **2017**, *1*, 0081. [CrossRef]

18. Chaparro, D.; Piles, M.; Vall-llossera, M.; Camps, A.; Konings, A.G.; Entekhabi, D. L-band vegetation optical depth seasonal metrics for crop yield assessment. *Remote Sens. Environ.* **2018**, *212*, 249–259. [CrossRef]
19. Attema, E.P.W.; Ulaby, F.T. Vegetation modeled as a water cloud. *Radio Sci.* **1978**, *13*, 357–364. [CrossRef]
20. Gao, Q.; Zribi, M.; Escorihuela, M.; Baghdadi, N.; Segui, P. Irrigation mapping using Sentinel-1 time series at field scale. *Remote Sens.* **2018**, *10*, 1495. [CrossRef]
21. Hagolle, O.; Huc, M.; Pascual, D.V.; Dedieu, G. A multi-temporal method for cloud detection, applied to FORMOSAT-2, VENμS, LANDSAT and SENTINEL-2 images. *Remote Sens. Environ.* **2010**, *114*, 1747–1755. [CrossRef]
22. Hagolle, O.; Huc, M.; Villa Pascual, D.; Dedieu, G. A multi-temporal and multi-spectral method to estimate aerosol optical thickness over land, for the atmospheric correction of formosat-2, Landsat, venμs and Sentinel-2 images. *Remote Sens.* **2015**, *7*, 2668–2691. [CrossRef]
23. Baghdadi, N.; Chaaya, J.A.; Zribi, M. Semiempirical calibration of the integral equation model for SAR data in C-band and cross polarization using radar images and field measurements. *IEEE Geosci. Remote Sens. Lett.* **2011**, *8*, 14–18. [CrossRef]
24. Baghdadi, N.; Choker, M.; Zribi, M.; Hajj, M.E.; Paloscia, S.; Verhoest, N.E.; Lievens, H.; Baup, F.; Mattia, F. A New Empirical Model for Radar Scattering from Bare Soil Surfaces. *Remote Sens.* **2016**, *8*, 920. [CrossRef]
25. Baghdadi, N.; Holah, N.; Zribi, M. Calibration of the integral equation model for SAR data in C-band and HH and VV polarizations. *Int. J. Remote Sens.* **2006**, *27*, 805–816. [CrossRef]
26. El Hajj, M.; Baghdadi, N.; Zribi, M.; Bazzi, H. Synergic use of Sentinel-1 and Sentinel-2 images for operational soil moisture mapping at high spatial resolution over agricultural areas. *Remote Sens.* **2017**, *9*, 1292. [CrossRef]
27. El Hajj, M.; Baghdadi, N.; Bazzi, H.; Zribi, M. Penetration Analysis of SAR Signals in the C and L Bands for Wheat, Maize, and Grasslands. *Remote Sens.* **2019**, *11*, 31. [CrossRef]
28. Wigneron, J.-P.; Jackson, T.J.; O'Neill, P.; De Lannoy, G.; De Rosnay, P.; Walker, J.P.; Ferrazzoli, P.; Mironov, V.; Bircher, S.; Grant, J.P. Modelling the passive microwave signature from land surfaces: A review of recent results and application to the L-band SMOS & SMAP soil moisture retrieval algorithms. *Remote Sens. Environ.* **2017**, *192*, 238–262.
29. Wigneron, J.-P.; Waldteufel, P.; Chanzy, A.; Calvet, J.-C.; Kerr, Y. Two-dimensional microwave interferometer retrieval capabilities over land surfaces (SMOS mission). *Remote Sens. Environ.* **2000**, *73*, 270–282. [CrossRef]
30. Baghdadi, N.; El Hajj, M.; Zribi, M.; Bousbih, S. Calibration of the Water Cloud Model at C-Band for Winter Crop Fields and Grasslands. *Remote Sens.* **2017**, *9*, 969. [CrossRef]
31. Gamon, J.A.; Field, C.B.; Goulden, M.L.; Griffin, K.L.; Hartley, A.E.; Joel, G.; Penuelas, J.; Valentini, R. Relationships between NDVI, canopy structure, and photosynthesis in three Californian vegetation types. *Ecol. Appl.* **1995**, *5*, 28–41. [CrossRef]
32. Running, S.W.; Nemani, R.R. Relating seasonal patterns of the AVHRR vegetation index to simulated photosynthesis and transpiration of forests in different climates. *Remote Sens. Environ.* **1988**, *24*, 347–367. [CrossRef]
33. Jones, M.O.; Jones, L.A.; Kimball, J.S.; McDonald, K.C. Satellite passive microwave remote sensing for monitoring global land surface phenology. *Remote Sens. Environ.* **2011**, *115*, 1102–1114. [CrossRef]
34. Jarlan, L. Inversion des données des diffusiomètres spatiaux pour le suivi de la végétation en zone semi-aride: Application au Sahel Africain. Ph.D. Thesis, Université Paul Sabatier Toulouse III, Toulouse, France, 2001.
35. Schroeder, R.; McDonald, K.C.; Azarderakhsh, M.; Zimmermann, R. ASCAT MetOp-A diurnal backscatter observations of recent vegetation drought patterns over the contiguous US: An assessment of spatial extent and relationship with precipitation and crop yield. *Remote Sens. Environ.* **2016**, *177*, 153–159. [CrossRef]
36. McNairn, H.; Duguay, C.; Brisco, B.; Pultz, T.J. The effect of soil and crop residue characteristics on polarimetric radar response. *Remote Sens. Environ.* **2002**, *80*, 308–320. [CrossRef]
37. Jiao, X.; Kovacs, J.M.; Shang, J.; McNairn, H.; Walters, D.; Ma, B.; Geng, X. Object-oriented crop mapping and monitoring using multi-temporal polarimetric RADARSAT-2 data. *ISPRS J. Photogramm. Remote Sens.* **2014**, *96*, 38–46. [CrossRef]
38. Vreugdenhil, M.; Wagner, W.; Bauer-Marschallinger, B.; Pfeil, I.; Teubner, I.; Rüdiger, C.; Strauss, P. Sensitivity of Sentinel-1 Backscatter to Vegetation Dynamics: An Austrian Case Study. *Remote Sens.* **2018**, *10*, 1396. [CrossRef]

39. Fieuzal, R.; Baup, F.; Marais-Sicre, C. Monitoring Wheat and Rapeseed by Using Synchronous Optical and Radar Satellite Data—From Temporal Signatures to Crop Parameters Estimation. *Adv. Remote Sens.* **2013**, *2*, 162. [CrossRef]
40. Ben-Ari, T.; Boé, J.; Ciais, P.; Lecerf, R.; Van der Velde, M.; Makowski, D. Causes and implications of the unforeseen 2016 extreme yield loss in the breadbasket of France. *Nat. Commun.* **2018**, *9*, 1627. [CrossRef]
41. Veloso, A.; Mermoz, S.; Bouvet, A.; Le Toan, T.; Planells, M.; Dejoux, J.-F.; Ceschia, E. Understanding the temporal behavior of crops using Sentinel-1 and Sentinel-2-like data for agricultural applications. *Remote Sens. Environ.* **2017**, *199*, 415–426. [CrossRef]
42. Njoku, E.G.; Chan, S.K. Vegetation and surface roughness effects on AMSR-E land observations. *Remote Sens. Environ.* **2006**, *100*, 190–199. [CrossRef]
43. Sawada, Y.; Koike, T.; Aida, K.; Toride, K.; Walker, J.P. Fusing microwave and optical satellite observations to simultaneously retrieve surface soil moisture, vegetation water content, and surface soil roughness. *IEEE Trans. Geosci. Remote Sens.* **2017**, *55*, 6195–6206. [CrossRef]